LSTM-NAS-Net: Enhanced Brain Tumor Segmentation in MRI and CT Images using LSTM-Autoencoder-based Neural Architecture Search

Santhosh Kumar[1,*], S. P. Sasirekha[2],R. Santhosh[3]

[1,2,3]Department of Computer Science and Engineering, Faculty of Engineering, Karpagam Academy of Higher Education
Coimbatore, Tamil Nadu, India

Emails: er.s.santhosh03@gmail.com; sugi.sasi29@yahoo.com; santhoshhrd@gmail.com

Abstract

Brain Tumour (BT) a mass or a lump or a growth which occurs due to abnormal cell division or unusual growth of cells in the brain tissue. Initially, the two major types of BT are Primary BT and Secondary BT, the tumour that originate from brain is known as Primary BT and it may be cancerous or non-cancerous. The tumour the initiates from other part of the body and spreads to the brain is stated as secondary BT. Diagnosing BT generally involves a multiple investigation method, such as MRI, CT, PET, SPECT as well as the neurological examinations and blood investigations, whereas some of the patients may need biopsies to evaluate the tumour size and stage. Here we use MRI and CT images for BT segmentation whereas these modalities play a major role in diagnosing, treating, planning and monitoring the BT patients. Moreover, the multimodal data can provide a quantitative information's about the tumour size, shape, volume and texture. While segmenting the BT the lack of segmentation methods and the interpretability of the segmented regions are limited. To overcome this, we propose a novel LSTM autoencoder bas NAS method which is used for the extracting the BT features and these features can be fused using Contextual Integration Module (CIM) and segmented using the Segmentation Guided Regulizer (SGR) which helps to overcome the stated issues. Finally, the performance metrices are calculated by comparing with the state-of -the -art methods and our method achieves a best segmenting metrices.

Keywords: Medical image Segmentation; Magnetic Resonance Imaging; CT; Unsupervised method; NAS.

1. Introduction

As one of the most important and fragile organs in the human body, the brain is especially prone to a wide range of disorders, the most serious of this organ was BT. Gliomas are among the most common BTs and have a high death rate. Low-grade gliomas (LGG) and high-grade gliomas (HGG) are the two primary subtypes of gliomas [1-2]. Because of their aggressive growth and fast nature, high-grade gliomas pose more hazards than low-grade counterparts and constitute a significant task. Approximately 86% to 92% of primary central nervous system (CNS) tumours are BTs. In 2021, 415,502 people were expected to have had a primary BT diagnosis worldwide. About 27,148 persons in the US, 18,446 of whom are men and 12,430 of whom are women, are expected to be diagnosed with primary malignant tumours of the brain in 2022. The lifetime probability of an individual having such tumours is

Doi : https://doi.org/10.54216/JCIM.140205
Received: January 17, 2024 Revised: March 18, 2024 Accepted: July 02, 2024

still less than 1% [3]. Cancers of the brain and nerve systems are the tenth largest cause of death in the world for both men and women. A variety of techniques are used to treat BT, such as radiation, surgery, and chemotherapy [4-5]. Applications for image analysis are widely used in many fields, from sensor network-based underwater imaging to terrestrial imaging. The timely detection of BTs is crucial in lowering death rates. One particularly important method for acquiring supplementary and comprehensive data regarding BTs is magnetic resonance imaging (MRI). T1-weighted, T2-weighted, T1c, and Flair are the four MRI modalities that provide strong information on the kinds of tumours that are there [6[. Precise surgery, follow-up analysis, and treatment planning all depend on accurate tumour structure segmentation. It also helps in the construction of tumour growth models, computer-based surgery, radiation therapy, tumour growth assessment, and treatment response evaluation [7[. BT segmentation by hand is labor-intensive and prone to mistakes. The intricacies involved highlight the necessity for continuous investigation and creativity to improve the efficiency of BT identification and management [8]. BT segmentation (BTS) and other medical picture segmentation tasks have advanced greatly using the combination of convolutional neural networks (CNNs) and vision transformers (ViTs) [9].

CNNs are frequently utilised because of their powerful feature representation capabilities, whereas ViTs are better at capturing long-range information in 3D volumetric data because they use self-attention techniques. ViTs have been modified in recent work to address issues like lesion location, morphological uncertainty, low contrast, and annotation bias in BT segmentation in 3D MRI sequences [10]. However, the successful integration of multi-modality images is a crucial component that is sometimes disregarded. While existing methods typically fuse modalities at either the input or feature level, recent Artificial Intelligence (AI) research emphasizes multi-modal fusion, particularly in establishing semantic connections between different modalities, such as images and language [11-13]. Computed Tomography (CT) imaging is readily accessible across hospitals and medical centers, ensuring patients requiring diagnostic assessment can promptly obtain scans [14]. This widespread availability expedites the process, enabling swift diagnosis and formulation of treatment plans for individuals suspected of harboring BT [15-16]. MRI and CT scans offer distinct insights into the brain and its composition. MRI excels in delineating soft tissue contrasts, rendering it ideal for discerning brain tumors and adjacent tissues. Conversely, CT imaging provides superior resolution for bone structures and calcifications. Integrating data from both modalities enhances the overall comprehension of tumor characteristics and its spatial relationship with neighboring structures [17].

Based on these observations, we present LSTM-NAS-Net, a novel neural network architecture search (NAS) based sampling module for BT feature extraction that uses LSTM-Autoencoder. This framework uses sequential medical imaging data to learn meaningful representations by utilising the power of LSTM-Autoencoder. This is a summary of our methodology: Ideal Prior to processing: First, we apply N4bias field correction and then we do several preprocessing techniques such as noise removal, intensity normalisation, skull stripping, Medila filtering, and picture enhancement. These procedures guarantee that the input data is suitably ready for further processing. The LSTM-NAS-Net Structure of our suggested architecture combines LSTM-NAS-Net with more extensive tumour segmentation algorithms. After being trained, the LSTM-Autoencoder functions as a feature extractor, extracting important spatial and temporal information from the input sequences that are pertinent to the imaging of BTs. Patterns indicating the presence, growth, shape, and texture of tumours may be among these traits. The NAS sampling module investigates and assesses several neural network designs that use these retrieved data to derive properties related to BTs. (i)Contextual Integration Module (CIM): We apply CIM approaches to efficiently integrate multi-modal information from MRI and PET images while maintaining spatial context. This guarantees that various brain regions are taken into account correctly, resulting in a segmentation that is more accurate. (ii)Segmentation-Guided Regularizer (SGR): Our system incorporates segmentation-guided regularisation approaches, which enable BT segmentation algorithms to take advantage of extra restrictions obtained from prior information or anatomical knowledge. Results from segmentation become more consistent and clinically significant as a result. Through the use of both spatial and temporal information from sequential medical imaging data, an optimised neural network architecture search process, contextual integration, and segmentation-guided regularisation techniques, our framework seeks to improve the accuracy and clinical relevance of BT segmentation.

A) Research Contributions:

- Here, the proposed LSTM based autoencoder can effectively extract the temporal features and by incorporating the NAS method in this autoencoder can design space to identify the architecture that maximize the feature extraction performance in the BT.

Doi : https://doi.org/10.54216/JCIM.140205
Received: January 17, 2024 Revised: March 18, 2024 Accepted: July 02, 2024

- The optimized neural architecture used in this framework can exhibit improved generalization and interpretability across the MRI and CT modalities which enhances the robustness and transferability in the feature extraction approach.
- The Fusion and segmentation method can elevate the spatial and contextual information and segmentation guidance to improve the accuracy in the BT segmentation.

B) Paper Organization:

The structure of the paper is outlined as follows: Section II offers a comprehensive review of prior research concerning tumor segmentation. In Section III, we provide an elaborate description of the research methodology utilized in the LSTM-NAS-Net framework. This section presents the architecture along with mathematical equations and diagrams to facilitate comprehension of the framework's operations. Section IV provides a short overview of the experimental results, including descriptions graphical representations of the performance metrics utilized and comparative analyses of the findings. Following that, Section V presents concluding remarks summarizing the key insights gathered from our work.

2. Related Works

Author in [18] suggests a hybrid Res-Net in conjunction with an optimised U-Net segmentation for precise BT MRI image categorization. The amalgamation of these methods improves tumour detection's effectiveness and precision, providing encouraging results for medical picture analysis. In [19] author provides an automated approach for identifying and categorising BT from MRI images using machine learning (ML) methods and the internet of things IoT. The technology delivers high tumour identification accuracy by using classical algorithms, which helps with early diagnosis and treatment planning. Author in [20] accurately identified BT from MRI data, a segmentation technique is used for deterministic feature clustering was obtained in this study. The suggested strategy expands segmentation accuracy by grouping informative characteristics, which helps to enhance neuroimaging diagnostic results. Author in [21] used a unique model named as Greedy Snake and Fuzzy C-Means Optimisation is given for automatically segmenting BT from MRI data. This technique effectively draws the borders of tumours, using fuzzy gathering to attain precise segmentation that supports medical diagnosis and therapy planning. In [22] As a Linear Complexity Data-Efficient Image Transformer for MRI BT classification, LCDEiT is presented. With its linear complexity and enhanced data efficiency, this model achieves better than others in tumour classification tasks, which discovers well for improvements in medical picture analysis and diagnosis. Author in [23] proposed a super pixel-based automated system for BT segmentation using MRI. The advised approach improves segmentation efficiency and accuracy by using super pixels, providing a feasible decision for accurate tumour delineation in medical imaging applications. Authors in [24] discussed about the utility of many deep transfer learning-based models for identifying BT from MRI is examined in this study. Tumour detection accuracy and reliability are increased through methodical experimentation and optimisation, which improves medical imaging's diagnostic skills. In [25] researched a method for segmenting BT using multimodal MRI data that incorporates edge information and deep semantics is proposed. The technique improves segmentation accuracy by combining these complimentary features, offering insightful information for tumour localization and classification in neuroimaging research. In [26] focused on precisely segmenting BT lesions using a 3D U-Net architecture. The work uses the ISLES 2018 dataset with the goal of improving tumour segmentation accuracy in medical imaging. The method donates to developments in BT diagnosis and therapy by refining the accuracy of recognising and crucial BT lesions by utilising 3D U-Net's capabilities. Authors in [27] identified a method for removing BT from CT scan pictures was presented in this paper. To improve tumour diagnosis and delineation, the method combines morphological dilation approaches with Prewitt edge detection. The suggested strategy combines several techniques to extract BT from CT scan data in an effective and exact manner, enabling early detection and treatment planning in neuroimaging.

In [28] explained that, by integrating Generative Adversarial Networks (GANs) and Variational Autoencoders (VAEs), this study suggests a unique method for classifying BT. The approach improves the robustness and accuracy of tumour classification in medical imaging by utilising the strengths of both architectures, perhaps leading to better diagnosis and treatment planning. In [29] introduced that an autoencoder convolutional neural network (CNN) for the purpose of segmenting BT. The autoencoder architecture is employed in this method to efficiently extract features from MRI images, which allows for precise tumour region segmentation. This method helps physicians locate and characterise tumours by showing encouraging outcomes in medical image analysis. Authors in [30] BrainNet

Doi : https://doi.org/10.54216/JCIM.140205
Received: January 17, 2024 Revised: March 18, 2024 Accepted: July 02, 2024

integrates stacked autoencoders with residual blocks to give a unique framework for multimodal BT classification. Through the combination of data from many modalities, the optional method recovers classification precision and resilience. This pattern presents a viable method for precise neuroimaging analysis diagnosis and therapy planning. The author proposed a approach for tumour diagnosis and impact analysis from 2-D MRI images, author presented a self-learning model based on variational autoencoders (VAEs). Through the use of VAEs, the model is able to learn tumour traits and their suggestions on its own, which helps with accurate tumour detection and analysis. This approach presents a potentially useful tool for improving diagnostic performance and comprehending tumour behaviour in medical imaging. It recovers segmentation accuracy and reliability by merging data from several modalities. With this method, brain metastases can be precisely identified, important to more accurate cancer diagnosis and treatment planning.

3. LSTM-NAS-Net Framework

This paper primarily addresses the refinement of brain tumor segmentation and the integration of multiple modalities, namely MRI and CT images. This study aims to enhance tumor detection accuracy through segmentation utilizing LSTM-based NAS. We have examined modalities of MRI and CT to emphasize the exploration of involved relationships among them. The proposed work includes two consecutive phases, namely, 1) data pre-processing and 2) LSTM-NAS-Net Framework and this section has two sub sections namely -Contextual Integration Module (CIM) and Segmentation-Guided Regularizer (SGR).

A) Data Pre-processing:

For precise diagnosis and treatment planning, BT segmentation from MRI and CT data is crucial. To enhance image quality and retrieve pertinent information for accurate BT detection, preprocessing of MRI and CT data is crucial. This optimal pre-processing method combines a number of techniques, including as intensity normalization, denoising, skull stripping, and N4 bias field correction. These procedures enhance the quality of CT and MRI scans and help with precisely segmenting and identifying the BT.

i) N4 Bias field correction:

The input data from CT and MRI scans is processed by the N4 Bias field correction and sophisticated normalizing tools. The intensity of the input image was eliminated, along with any variance brought about by the acquisition process's differences. By adjusting the estimated bias field in the original field, the N4 Bias uses a combination of low pass filter and B-spline to correct the intensity of the MRI and CT data. The adjusted intensity is equivalent to:

$$\mathcal{C}_{\mathcal{J}}[\mathcal{V}] = \frac{\mathcal{C}[\mathcal{V}]}{\mathcal{B}[\mathcal{V}]} \quad (1)$$

Where,
$\mathcal{C}_{\mathcal{J}}[\mathcal{V}]$ is noted as the corrected intensity at the voxel $\mathcal{V}$. $\mathcal{C}[\mathcal{V}]$ is denoted as the original intensity of the voxel $\mathcal{V}$. The estimated bias field at the voxel $\mathcal{V}$ is noted as $\mathcal{B}[\mathcal{V}]$.

ii) Denoising:

The MRI and CT images are denoised utilizing the median and bilateral filtering approaches after the bias correction. By replacing each pixel's value with the neighboring value of the median value, the median filtering approach reduces noise in MRI scans. The value of parameter $\mathcal{P}$ determines the size of the median filter window, and the neighboring pixel indices indicated by. The capacity of median filtering to lower noise in MRI images without compromising edge integrity is highly appreciated, as it is essential for precisely identifying and classifying brain cancers. This filtering technique efficiently improves the quality of MRI images, which makes it easier to retrieve important information needed for accurate diagnosis and therapy planning for BT.

$$\mathcal{C}_{\mathcal{J}_{MED}}(\mathcal{K}, \mathcal{L}) = med\ \mathcal{C}(\mathcal{K} + \mathcal{T}^1, \mathcal{L} + \mathcal{T}^2), \mathcal{K}, \mathcal{L} \in [-\mathcal{P}, \mathcal{P}] \quad (2)$$

The window size of the filter is noted by $\mathcal{P}$, and the adjacent pixels indices are represented by $\mathcal{T}^1$, $\mathcal{T}^2$. Following the MRI denoising the CT image uses the bilateral filtering and this denoising is equated by,

$$\mathcal{C}_{\mathcal{J}_{BIL}}(\mathcal{K}, \mathcal{L}) = \frac{1}{\mathcal{NF}} \sum_{\mathcal{T}^1=-\mathcal{P}}^{\mathcal{P}} \sum_{\mathcal{T}^2=-\mathcal{P}}^{\mathcal{P}} \mathcal{C}(\mathcal{K} + \mathcal{T}^1, \mathcal{L} + \mathcal{T}^2) \varphi_{\mathcal{T}^1, \mathcal{T}^2} \quad (3)$$

Here, $\mathcal{NF}$ indicates the normalization factor.

iii) Skull stripping and intensity normalization:

Doi : https://doi.org/10.54216/JCIM.140205
Received: January 17, 2024 Revised: March 18, 2024 Accepted: July 02, 2024

Variations in intensity levels and non-brain tissues that could otherwise obstruct the investigation of tumor regions are efficiently reduced by combining intensity normalization with skull stripping. Along with the intensity normalization, the equation is used as follows:

$$\mathcal{C}_{\mathcal{Z}}(\mathcal{K}, \mathcal{L}) = \frac{\mathcal{C}(\mathcal{K}, \mathcal{L}) - \sigma}{\rho} \quad (4)$$

σ and ρ are the specifications that serve as a representation of the mean and standard deviation of the intensity values over the whole image are computed using this equation. The Z-score normalization is utilized to standardize the intensity levels of MRI images to a shared range, applying it to every pixel. To reduce intensity value changes, the mean and standard deviation of the total image are used in this method. The quality of MR images is improved by normalizing these intensity values, making it easier to obtain relevant information that is essential for accurately detecting and grading brain lesions. The process of skull stripping, which involves extracting non-brain tissues from MRI data, is carried out using the mathematical equations given in Equation 5. In order to differentiate brain tissue from non-brain tissues, the equations incorporate edge detection and thresholding techniques, producing a binary mask that defines the brain tissue. Because the presence of non-brain tissues can skew the analysis of tumor regions, this stage is essential for the accurate detection and segmentation of brain tumors. Skull stripping, a method of removing non-brain tissues from MRI scans, enhances the images' quality and helps with precise diagnosis and treatment plans for BT.

$$\mathfrak{M}(\mathcal{K}, \mathcal{L}) = \{1 \; if \; \mathcal{C}(\mathcal{K}, \mathcal{L}) > j0 \text{ otherwise} \quad (5)$$

Following the MRI Skull stripping and intensity normalization the CT image also undergoes the same process, respectively.

B) LSTM-NAS-Net Framework:

The ability of Long Short-Term Memory (LSTM) networks to analyze sequential data is well known. They are skilled at jobs requiring temporal comprehension because they are good at combining both past and current information from a sequence. An LSTM unit can identify long-range dependencies in a sequence because it receives inputs at each step that include both the historical context and the current data point $\mathbb{T}_{\mathrm{i}}$ and it is the memory unit and hidden state at a specific timestep $\mathbb{T}_{\mathrm{i}} - 1$ and the input state at a particular time step $\mathbb{T}_{\mathrm{i}}$. Forget gate, input gate, and output gate are the three components that make up an LSTM unit. The forget gate is used to calculate its output, which may be represented as follows, and use that result to choose whether to use historical data:

$$\mathcal{FOR}_{\mathbb{T}_{\mathrm{i}}} = Sig(i\mathcal{p}_{\mathbb{T}_{\mathrm{i}}} \mathfrak{we}_{\mathfrak{x}\mathfrak{F}} + \hbar i_{\mathbb{T}_{\mathrm{i}}-1} \mathfrak{we}_{\mathfrak{H}\mathfrak{F}} + \mathcal{b}i_{\mathfrak{F}} \quad (6)$$

where $\mathcal{FOR}_{\mathbb{T}_{\mathrm{i}}}$ The term represents the output of the forget gate, $i\mathcal{p}_{\mathbb{T}_{\mathrm{i}}}$ indicates the input at time $\mathbb{T}_{\mathrm{i}}$, $\hbar i_{\mathbb{T}_{\mathrm{i}}-1}$ is noted by the hidden state at time $\mathbb{T}_{\mathrm{i}} - 1$, and $\mathfrak{we}_{\mathfrak{x}\mathfrak{F}}$, $\mathfrak{we}_{\mathfrak{H}\mathfrak{F}}$, and $\mathcal{b}i_{\mathfrak{F}}$ signify the respective weights and bias. The input gate determines how much current state information should be kept, and the following is how its output is calculated:

$$\mathcal{I}_{\mathbb{T}_{\mathrm{i}}} = sig(i\mathcal{p}_{\mathbb{T}_{\mathrm{i}}} \mathfrak{we}_{\mathfrak{x}\mathcal{I}} + \hbar i_{\mathbb{T}_{\mathrm{i}}-1} \mathfrak{we}_{\mathfrak{H}\mathcal{I}} + \mathcal{b}i_{\mathcal{I}} \quad (7)$$

The output gate is closely tied to the hidden state $\hbar i_{\mathbb{T}_{\mathrm{i}}}$ and its output is determined through the following calculation.:

$$\mathcal{OP}_{\mathbb{T}_{\mathrm{i}}} = sig(i\mathcal{p}_{\mathbb{T}_{\mathrm{i}}} \mathfrak{we}_{\mathfrak{x}\mathcal{OP}} + \hbar i_{\mathbb{T}_{\mathrm{i}}-1} \mathfrak{we}_{\mathfrak{H}\mathcal{OP}} + \mathcal{b}i_{\mathcal{OP}} \quad (8)$$

$\boldsymbol{\mathcal{CA}}_{\mathbb{T}_{\mathrm{i}}}$ is named a memory unit, and $\widehat{\boldsymbol{\mathcal{CA}}}_{\mathbb{T}_{\mathrm{i}}}$ is the candidate memory; their standards can be reorganized as follows:

$$\widehat{\boldsymbol{\mathcal{CA}}}_{\mathbb{T}_{\mathrm{i}}} = \tan \mathcal{Z}(\, i\mathcal{p}_{\mathbb{T}_{\mathrm{i}}} \mathfrak{we}_{\mathfrak{x}\boldsymbol{\mathcal{CA}}} + \hbar i_{\mathbb{T}_{\mathrm{i}}-1} \mathfrak{we}_{\mathfrak{H}\boldsymbol{\mathcal{CA}}} + \mathcal{b}i_{\boldsymbol{\mathcal{CA}}} \quad (9)$$

$$\boldsymbol{\mathcal{CA}}_{\mathbb{T}_{\mathrm{i}}} = \mathcal{FOR}_{\mathbb{T}_{\mathrm{i}}} \gamma \boldsymbol{\mathcal{CA}}_{\mathbb{T}_{\mathrm{i}}-1} + \mathcal{I}_{\mathbb{T}_{\mathrm{i}}} \gamma \widehat{\boldsymbol{\mathcal{CA}}}_{\mathbb{T}_{\mathrm{i}}} \quad (10)$$

where the operator γ is the multiplication of matrices results in the final step, yielding the calculation for the output of the hidden state.

$$\hbar i_{\mathbb{T}_{\mathrm{i}}} = \mathcal{OP}_{\mathbb{T}_{\mathrm{i}}} \gamma \tan \mathcal{Z}(\boldsymbol{\mathcal{CA}}_{\mathbb{T}_{\mathrm{i}}}) \quad (11)$$

An unsupervised learning method called autoencoders is used to rebuild input data. The encoder compresses the input into a lower-dimensional latent space while acting as a feature extractor inside an encoder-decoder system.

Doi : https://doi.org/10.54216/JCIM.140205
Received: January 17, 2024 Revised: March 18, 2024 Accepted: July 02, 2024

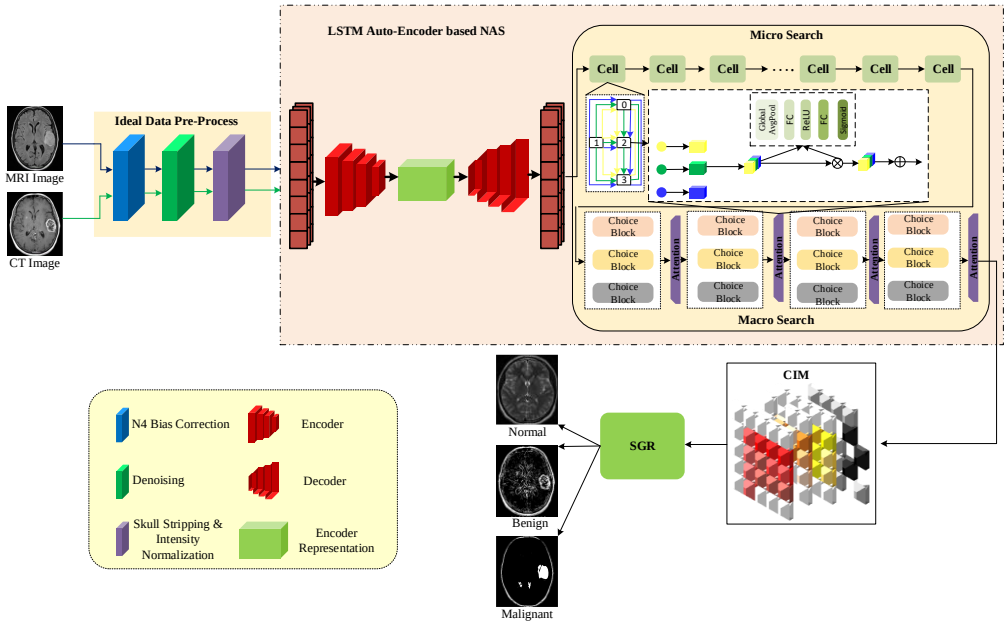

Figure 1: Represents the overall Architecture of the LSTM-NAS-Net

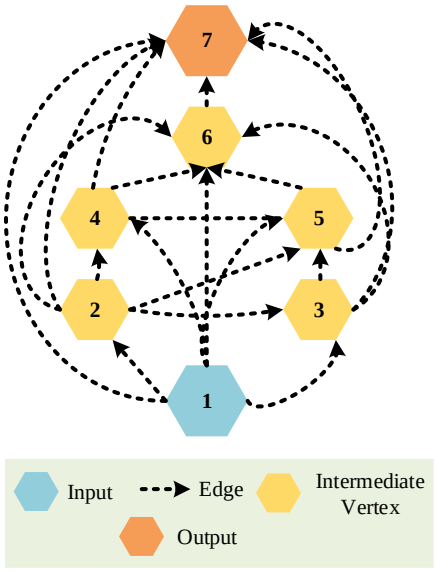

Figure 2: Outline of cell-based Micro search space.

On the other hand, the decoder serves as a reconstructive component, whose job it is to retrieve the input data from the hidden space. Autoencoders are often constructed using bottleneck network designs to extract low-dimensional representations from input data. The goal is to minimize reconstruction loss in the context of imaging inputs so that the reconstructed sequence can capture the distribution of inputs. Specifically, the segmentation of imaging data presents a difficulty for reconstruction, and because of its complexity, reconstruction mistakes are increased. Considering that LSTMs are good at extracting sequence information and autoencoders are useful for detecting outliers in sequences, their combination could be useful for efficiently locating outliers in sequences. The suggested method for brain tumor segmentation combines LSTM-autoencoder-based NAS with specially designed macro and micro search areas. Neural network architecture discovery and optimization are automated using NAS. The hyperparameters that determine how each individual cell is configured are located in the cell-based micro search space, while two more hyperparameters are found in the macro search space.

Doi : https://doi.org/10.54216/JCIM.140205
Received: January 17, 2024 Revised: March 18, 2024 Accepted: July 02, 2024

C) Micro and Macro Search space:

To find the LSTM design that is best at extracting features from BT data, NAS involves navigating a range of possible LSTM architectures. Performance indicators such as reconstruction accuracy or the ability of retrieved features to discriminate between different types of tumors can guide this investigation. The encoder and decoder cells of the design are in charge of up sampling and down sampling, respectively. After a series of convolution operations for feature extraction, encoder cells maxpool with a stride of 2 to reduce the image size. On the other hand, transpose convolution is used by decoder cells to increase the input size as they reconstruct the image using the information that the encoder cells extracted. Fig 2: Outline of cell-based Micro search space. The architecture in a micro search space designed for NAS in BT feature extraction from MRI and CT scans is broken down into more manageable, reusable components called cells. Each cell consists of an assemblage of connections and activities that enable the construction of multiple architectures. processes are sequentially organized within each cell and then added element-by-element to integrate the results of various processes. Through sifting through these cells to find the best possible combinations of operations and connections, NAS may independently identify architectures that are skilled at extracting features from MRI and CT scans for BT segmentation. Higher segmentation accuracy and improved generalization performance are the outcomes of this approach. Similarly, in the NAS-tailored macro search space for brain tumor extraction from MRI and CT scans, the focus is on creating large-scale architectural structures with linked cells. The overall architecture is built via a hierarchically organized sequence of processes hosted by each cell. These operations retrieve relevant features that are necessary for segmentation from the input data by examining different aspects of the data. Because of the hierarchical arrangement of cells, features obtained from lower-level counterparts are integrated into upper-level cells. The micro and macro cell based nth output of each cell is considered by:

$$\mathbb{D}_{\mathbb{I}} = \sum_{\forall-1}^{\partial} \mathfrak{f}\mathfrak{n}_{\forall}(\mathcal{WE}_{\mathbb{I}\forall} \times \mathfrak{r}) \qquad (12)$$

$\mathbb{D}_{\mathbb{I}}$ as the output of the $\mathbb{I}$ th cell in the architecture. $\mathfrak{O}_{\forall\mathbb{I}}$ as the $\forall$ operation in the $\mathbb{I}-$ th cell. $\mathfrak{f}\mathfrak{n}_{\forall}$ as the function corresponding to operation $\mathfrak{O}_{\forall\mathbb{I}}$, $\mathcal{WE}_{\mathbb{I}\forall}$ as the weights associated with operation $\mathfrak{O}_{\forall\mathbb{I}}$, $\mathfrak{r}$ as the input feature map. The network is able to understand both local and global context because to this hierarchical architecture, which is essential for accurate segmentation. By exploring networked cells in a macro search space, NAS can find structures on its own that are optimized for BT segmentation feature extraction from MRI and CT data. This approach speeds up the process of creating segmentation models that are able to capture both fine-grained details and broad context, which leads to improved segmentation accuracy. In the conclusion, our unique feature extraction method shows resilience when processing MRI and CT scans, successfully extracting features in an unsupervised manner while maintaining temporal relationships.

i) Contextual Integration Module (CIM)

Our Contextual Integration Module (CIM) can adapt its focus by being severely aware of different image modalities respond to different places. To improve the segmentation accuracy the extraction of discriminative features unique to tumor regions is made possible by this nuanced technique. In order to accomplish this, we provide the CIM module, which smoothly incorporates modal elements into the context of each region. CIM and probability map learning are the two main parts of the CIM module.

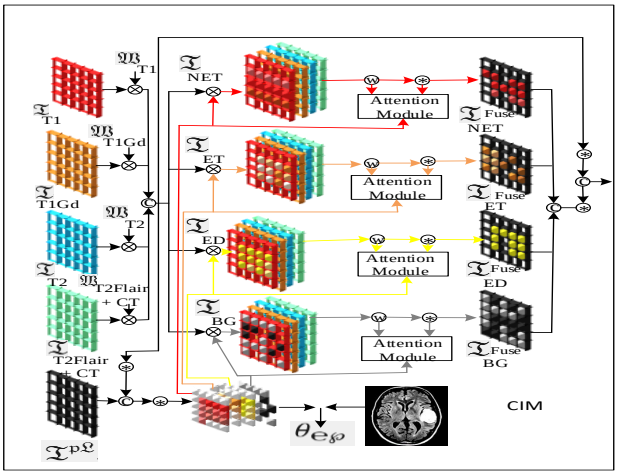

Figure 3: Displays the Contextual Integration module with the probability map and attention mechanisms.

Doi : https://doi.org/10.54216/JCIM.140205
Received: January 17, 2024 Revised: March 18, 2024 Accepted: July 02, 2024

Probability map learning

The probability map is created by taking data from the previous layer's decoder feature $\mathfrak{T}^{\mathfrak{p}\mathfrak{Q}}$, and the available encoder features$\nexists_{\wp\mathfrak{t}\mathfrak{w}}[\mathfrak{T}^{\wp}.\mathfrak{W}^{\wp}]$. The accuracy of the probability maps is improved by improving spatial granularity through the integration of encoder characteristics into the CIM approach. Including MRI and CT the symbol $\nexists$ represents concatenation, while the character $\mathfrak{w}$ represents the modalities that are included, $\mathfrak{W}^{\wp}$ takes on values of 0 or 1 indicating whether the $\wp$ modality is present or not. This formal outline of the probability map learning process is as follows:

$$\alpha_{\mathfrak{h}\mathfrak{r}}^{\mathfrak{e}\wp}=\frac{\exp(\aleph_{\mathfrak{r}}(\mathfrak{T}_{\mathfrak{h}\mathfrak{r}}^{\mathfrak{e}\wp};\pi_{\mathfrak{r}}))}{\mho_{\mathcal{g}}\mathcal{E}_{\mathcal{g}}\exp(\aleph_{\mathfrak{r}}(\mathfrak{T}_{\mathfrak{h}\mathfrak{r}}^{\mathfrak{e}\wp};\pi_{\mathfrak{r}}))} \qquad (13)$$

Where the features $\mathfrak{T}_{\mathfrak{h}\mathfrak{r}}^{\mathfrak{e}\wp}$ are obtained from $\mathfrak{T}_{\mathfrak{h}\mathfrak{r}}^{\mathfrak{p}\mathfrak{Q}}$ and$\nexists_{\wp\mathfrak{t}\mathfrak{w}}[\mathfrak{T}_{\mathfrak{h}\mathfrak{r}}^{\wp}.\mathfrak{W}^{\wp}]$. In this case, $\mathfrak{h}$ stands for $\mathfrak{h}$ -th subject and $\mathfrak{r}$ for the $\mathfrak{r}$ -th network stage or level. The expected probability map is denoted as $\alpha_{\mathfrak{h}\mathfrak{r}}^{\mathfrak{e}\wp}$. The region classifier at stage $\mathfrak{r}$ is represented by$\aleph\mathfrak{r}$, with related parameters$\pi_{\mathfrak{r}}$. The set δ contains the region of interest in BT such as BG, NCR/NET, ED, and ET. The probability map is learned under the supervision of the ground truth by a weighted cross entropy lossρ_{WXC} and a Dice lossρ_{DIL}, expressed as:

$$\rho_{\mathrm{B}\upsilon}=\sum_{\mathfrak{h}-1}^{\phi}\sum_{\mathfrak{r}-1}^{\mu}(\rho_{WXC}(\theta_{\mathfrak{r}}(\alpha_{\mathfrak{h}\mathfrak{r}}^{\mathfrak{e}\wp}),\mathfrak{K}_{\mathfrak{h}})+\rho_{DIL}(\theta_{\mathfrak{r}}(\alpha_{\mathfrak{h}\mathfrak{r}}^{\mathfrak{e}\wp}),\mathfrak{K}_{\mathfrak{h}})) \qquad (14)$$

Where ϕ and μ denotes the number of training data and stages. $\theta_{\mathfrak{r}}$denotes the up-sampling operation in the$\mathfrak{r}$ -th stage, aiming to match the resolution of the probability map $\alpha_{\mathfrak{h}\mathfrak{r}}^{\mathfrak{e}\wp}$ and the ground-truth mask $\mathfrak{K}_{\mathfrak{h}}$. $\rho_{WXC}$is formulated as:

$$\rho_{WXC}(\alpha,\mathfrak{K})=\sum_{\mathcal{g}\mathcal{E}\delta}\frac{\Psi-\mathfrak{B}_{\mathcal{g}}.\mathfrak{K}_{\mathcal{g}}.\log(\alpha_{\mathcal{g}})\Psi_{1}}{\mathbb{G}.\mathbb{M}.\mathbb{P}} \qquad (15)$$

Where $\mathbb{G}.\mathbb{M}.\mathbb{P}$ represent the width, height, and slice number of the three-dimensional volumes and Ψ ,$\Psi_1$signifies the L1 norm. The weight of the region $\mathcal{g}$ is denoted by$\mathfrak{B}_{\mathcal{g}}$. The formulation of LDL is:

$$\rho_{DIL}(\alpha,\mathfrak{K})=1-\sum_{\mathcal{g}\mathcal{E}\delta}\frac{2.\Psi\alpha_{\mathcal{g}}\mathfrak{Q}\mathfrak{K}_{\mathcal{g}}\Psi_{1}}{\delta_{num}.(\Psi\alpha_{\mathcal{g}}\Psi_{1}+\Psi\mathfrak{K}_{\mathcal{g}}\Psi_{1})} \qquad (16)$$

Where $\mathfrak{Q}$ represents the overlap between predictions and ground-truth masks, and δ_{num} represents the number of regions in δ. CIM has successfully divided multi-modal features into distinct regions by utilizing the probability map. Consequently, region-aware fusion is performed on the subdivided characteristics within each region. By the probability map the feature division is implemented by multiplying features, the following formula is:

$$\mathfrak{T}_{\mathcal{g}}=\nexists_{\wp\mathfrak{t}\mathfrak{w}}[\mathfrak{T}^{\wp}.\mathfrak{W}^{\wp}].\alpha_{\mathcal{g}}^{\mathfrak{e}\wp} \qquad (17)$$

Where $\mathfrak{T}_{\mathcal{g}}$ represents the divided features of the available modalities in the tumor region $\mathcal{g}$ and $\mathfrak{T}^{\wp}$ represents the encoder feature of the modality $\wp$. After the features have been divided, to merge the corresponding features distinct attention weights are trained for each modality across multiple regions. The procedure is the attention weight which generated for region$\mathcal{g}$. During this procedure the global characteristic of region $\mathcal{g}$ is subjected to an average pooling operation and then normalized using the probability map$\alpha_{\mathcal{g}}^{\mathfrak{e}\wp}$. It is possible to mitigate the risk of the global feature becoming overly small numerically by employing region-normalized pooling, which is a consequence of the typically small area that brain tumors occupy within the brain. A subsequent set of transformations is implemented to encode the normalized feature as modal-specific attention weights that consist of two fully connected layers, a Leaky ReLU layer, and a sigmoid activation. Later, the attention weights are implemented to modify the means in which the divided feature $\mathfrak{T}_{\mathcal{g}}$ incorporates available modalities which results in the generation of discriminative fused features. By employing unique attention modules CIM accounts for the distinct sensitivities that exist between regions and modalities which evaluate attention weights corresponding to each region. CIM is able to capture more comprehensive features for every region by giving priority to modalities that are exceptionally sensitive. The decoder is supplied with these region-specific characteristics by concatenation and a convolutional bottleneck. In addition, CIM incorporates a shortcut connection similar to residual learning for improved performance.

Doi : https://doi.org/10.54216/JCIM.140205
Received: January 17, 2024 Revised: March 18, 2024 Accepted: July 02, 2024

Segmentation Guided Regulizer (SGR)

A contrast in training frequently results from the lack of multi-modal data, specifically in the context of deep neural networks. By employing discriminative modalities, the primary objective of these networks is to segment tumor regions. Whereas others have difficulty doing so certain modal encoders therefore excel at localizing tumor regions. The lack of critical modalities can substantially decrease the accuracy of tumor segmentation because of this imbalance. As a solution to this problem, we have proposed the SGR which designed for segmentation purposes. To segment individual modal images, CIM employs a decoder,$\Im_{DUP}$, which shares weights. In the following formulation, the regularization term is comprised of weighted cross-entropy loss and Dice loss:

$$\theta_{\mathrm{RE}} = \sum_{\mathfrak{h}-1}^{\phi} \sum_{\mathfrak{r}-1}^{\mu} (\rho_{WXC}(\theta_{\mathfrak{r}}(\alpha_{\mathfrak{h}\mathfrak{r}}^{DUP}), \Re_{\mathfrak{h}}) + \rho_{DIL}(\theta_{\mathfrak{r}}(\alpha_{\mathfrak{h}\mathfrak{r}}^{DUP}), \Re_{\mathfrak{h}})) \quad (18)$$

$\alpha_{\mathfrak{h}\mathfrak{r}}^{DUP}$,$\mathfrak{h}\mathfrak{r}$represents the segmentation mask prediction derived from modality $\mathfrak{r}$ for the $\mathfrak{h}$ th subject. The SGR instructs that every modal encoder is capable of differentiating distinct tumor regions. In segmentation this method passes CIM in attaining encoder features which was more significant and resulting in improved accuracy.

General Loss

θ_{FS} executes to predict the final segmentation mask by combining the features. We utilize a combination of Dice loss and weighted cross-entropy loss to align these forecasts with the corresponding ground-truth segmentation maps, in the following manner:

$$\theta_{\mathrm{FS}} = \sum_{\mathfrak{h}-1}^{\phi} \rho_{WXC}(\theta_{\mathfrak{r}}(\alpha_{\mathfrak{h}}^{FS}), \Re_{\mathfrak{h}}) + \rho_{DIL}(\theta_{\mathfrak{r}}(\alpha_{\mathfrak{h}}^{FS}), \Re_{\mathfrak{h}})) \quad (19)$$

Where $\alpha_{\mathfrak{h}}^{FS}$is the segmentation mask predicted for the $\mathfrak{h}$ -th subject. Therefore, the comprehensive loss of our CIM is drawn as:

$$\theta = \theta_{\mathrm{e}_{\mathfrak{s}\wp}} + \theta_{RE} + \theta_{FS} \quad (20)$$

4. Experimental Results

i) Dataset details:

The dataset comprises a substantial collection of annotated MRI scans of brain tumors, primarily sourced from The Cancer Imaging Archive. As the validation and test datasets in the BraTS challenge 2021 Dataset remain undisclosed, we partitioned the training set, consisting of 1251 3D MRI images, provided by the challenge organizers for all experimental purposes. The dataset consists of 834 samples in the training set, 208 in the validation set, and 209 in the test set. All MRI images underwent skull stripping and resampling to a resolution of 1mm^3. Each patient's MRI comprises four modalities: T1-weighted (T1), post-contrast T1-weighted (T1Gd), T2-weighted (T2), and T2 Fluid Attenuated Inversion Recovery (T2FLAIR), all co-registered to a T1 anatomical template. The annotations are categorized into three distinct sub-regions: Gd-enhancing tumor (ET), peritumoral edematous invaded tissue (ED), and necrotic tumor core (NCR). Following the recommendations of the challenge organizers, these subregions are further grouped into three segmentation-friendly regions for evaluating segmentation performance: enhanced tumor (ET), tumor core (TC) (which combines ET and NCR), and whole tumor (WT) (which encompasses ED and TC). The Cancer Genome Atlas (TCGA) Lower Grade Glioma (LGG) dataset encompasses molecular and clinical data derived from individuals diagnosed with lower grade gliomas, a subtype of BT. This dataset incorporates diverse information sources, including CT scans, to provide comprehensive insights into glioma pathology. It's noteworthy that CT scans are less prevalent in brain tumor imaging compared to MRI.

ii) Stimulation Environment:

The network is implemented in PyTorch and trained on an NVIDIA RTX 3090 GPU equipped with 64 GB of video memory. A batch size of 1 is employed, and training commences from scratch for 400 epochs. The Adam optimizer is utilized, with the initial learning rate configured to 0.001. During preliminary assessments, direct training of the model was found to be time-consuming. Therefore, for this experiment, a pre-trained model is employed instead.

iii) *Evaluation metrices*:

To assess the efficiency of the proposed LSTM-NAS-Net models, we used metrics including the Dice Similarity Coefficient (DSC), Sensitivity, Specificity, and Accuracy as key indicators of performance. These metrics can be

Doi : https://doi.org/10.54216/JCIM.140205
Received: January 17, 2024 Revised: March 18, 2024 Accepted: July 02, 2024

expressed using TP, FP, TN, and FN, representing the counts of true positives, false positives, true negatives, and false negatives, respectively. The formulations for these metrics are as follows:
Dice score coefficient:

$$\text{DSC} = \frac{2\times\mathcal{TAR}\cap\mathcal{PRE}}{\mathcal{TAR}+\mathcal{PRE}} \quad (21)$$

This calculation involves an overlap-based metric used to quantify the spatial agreement between the ground truth mask and the predicted mask. Where $\mathcal{TAR}$ represented the target tumour and $\mathcal{PRE}$ means the prediction.
Sensitivity:

$$\text{Sensitivity} = \frac{\mathbb{T}_{\mathbb{POS}}}{\mathbb{T}_{\mathbb{POS}}+\mathbb{F}_{\mathbb{NEG}}} \quad (22)$$

It represents the proportion of true positive values correctly identified. Here $\mathbb{T}_{\mathbb{POS}}$ designates the true positive and $\mathbb{F}_{\mathbb{NEG}}$ indicates the false negative.
Specificity:

$$\text{Specificity} = \frac{\mathbb{T}_{\mathbb{NEG}}}{\mathbb{T}_{\mathbb{NEG}}+\mathbb{F}_{\mathbb{POS}}} \quad (23)$$

It denotes the percentage of true negative values correctly identified. $\mathbb{T}_{\mathbb{NEG}}$ shows the true negative and $\mathbb{F}_{\mathbb{POS}}$ is noted as false positive.
Accuracy:
This metric is a probabilistic measure assessing the level of agreement between the segmentation outcomes and the ground truth segmentation mask.

$$\text{Accuracy} = \frac{\mathbb{T}_{\mathbb{POS}}+\mathbb{T}_{\mathbb{NEG}}}{\mathbb{T}_{\mathbb{POS}}+\mathbb{T}_{\mathbb{NEG}}+\mathbb{F}_{\mathbb{POS}}+\mathbb{F}_{\mathbb{NEG}}} \quad (24)$$

iv) Comparison with various network frameworks using the BRATS 2021 dataset:

Table 1 shows the comparison of our proposed method with state-of-the-art-methods like BrainNet [30], LCDEIT [22], SegNet [20] on the 2021 BRATS dataset. Following that the complete, Core, Enhancing indicates the DSC of the WT, TC, ET.

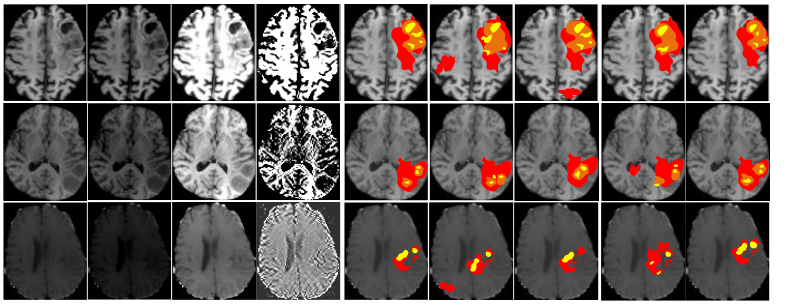

Figure 4: shows the quantitative comparison and visualization on BRATS2021 dataset. From top to bottom are BRATS 1197, BRATS 73, BRATS1395

Moreover, the results show an outstanding performance compared with the other frameworks, whereas we use a flexible method for feature extraction and it can explore the integration of the LSTM with NAS and it effectively maximize the DSC thus it allows the model to be more adaptive. Figure 4 shows the quantitative comparison and visualization on BRATS2021 dataset. From top to bottom are BRATS 1197, BRATS 73, BRATS1395 respectively. The Red, Brown, Yellow designates the ED (Effective Diameter), ET (Enhancing Tumor), and NCR (Non-Contrast Region). By analysing the quantitative comparison, it declares that it was helpful in gaining valuable understanding the tumor characteristics, aggressiveness and treatment response.

Table 1: Shows the Comparison with the existing method with our method on BRATS 2021 dataset. The Complete, Core, Enhancing indicates the DSC of the WT, TC, ET, respectively.

Modalities	DSC (%)		
	Complete	Core	Enhancing

Doi : https://doi.org/10.54216/JCIM.140205
Received: January 17, 2024 Revised: March 18, 2024 Accepted: July 02, 2024

	Brain Net	LCDEIT	SegNet	Our method	Brain Net	LCDEIT	SegNet	Our method	Brain Net	LCDEIT	SegNet	Our method
T2 Flair												
●	85.26	86.24	86.94	87.36	69.25	70.96	71.22	72.68	45.55	46.25	47.21	47.69
◦	76.32	75.20	76.98	77.25	79.99	80.26	81.30	82.45	74.20	73.96	75.01	75.68
◦	76.96	75.03	77.87	78.21	65.35	66.95	64.26	67.25	38.96	37.55	38.20	39.47
◦	85.99	86.21	87.36	88.24	68.48	69.55	67.21	70.26	38.21	38.65	39.22	40.99
●	86.78	87.36	88.12	88.97	82.33	83.99	83.66	84.96	74.99	75.88	75.98	76.98

Figure 5 shows the ET, TC, and WT performance in DSC, Sensitivity, Specificity and Accuracy of our method. The distribution features of the outcomes for the four evaluation indicators in the training and test sets are shown by the box plots and scatter plots. Understanding the distribution of performance indicators across the datasets and the trends and variability in the evaluation results is made easier with the help of these representations. The box plot indicates that the findings exhibit less variation and that there are fewer outliers across the different variables. The dataset's median is shown by the horizontal line in the box plot. It is evident that the Dice, Sensitivity, Accuracy, and Specificity of the three indicators are at high values.

This implies that our suggested model's segmentation effectiveness is located in a greater range. The sensitivity of each of the four indicators consistently demonstrates concentrations at greater levels. Interestingly, there isn't much variation seen in its range. It is clear from looking at the scatter diagram on the left that the data are primarily grouped at higher locations. This implies that our model successfully anticipates a high level in the background, hence reducing the problem of foreground and background pixel imbalance. Here, table 2 shows the overall performance metrices of the state-of-the-art-methods with our method. By comparing with the other models using BRATS2021 dataset, our metho shows a unique quantitative improvement. LSTM-NAS-Net has shown a finest segmentation performance because it has an ability to generalize and enhance the robustness and ensures the consistent among the MRI modality. LSTM autoencoder based NAS is a powerful method segmenting BT and leads to attain a improved accuracy, sensitivity and specificity.

Doi : https://doi.org/10.54216/JCIM.140205
Received: January 17, 2024 Revised: March 18, 2024 Accepted: July 02, 2024

Table 2: shows the overall performance metrices of the state-of-the-art-methods with our method

Methods/ Metrices	Specificity			Sensitivity			Accuracy		
	ET	TC	WT	ET	TC	WT	ET	TC	BT
BrainNet	94.25	93.65	96.58	95.21	91.63	92.33	96.13	91.83	95.36
LCDEIT	94.99	94.56	95.68	96.74	96.52	95.23	94.20	92.26	96.33
SegNet	95.63	94.98	96.71	96.73	97.53	95.37	96.07	94.67	97.63
Our method	96.32	95.73	97.66	97.21	98.66	96.83	97.33	95.81	98.36

v) Comparison with various network frameworks using the MRI and CT images:

The MRI and CT image fusion is assessed with the existing methods like AD-Net [34], DL-Net [35], AutoNet [36], CrossNet [37], Improved-U-Net [38]. Our fusion module has increased robustness to variability and our module learns to weight adaptively and makes the segmentation less sensitive. Table: 3 shows the comparison of The MRI and CT image fusion is assessed with the existing method. Figure 6: shows the outperformed conventional approaches in terms of quantitative performance. Our fusion of multi-modality will learn the complementary features that captures the various features of morphology of tumour and thus other existing models lacks in concentrating the MRI and CT fusion. Fig 7: represents the MRI-CT fusion. Comparison with various network frameworks using the MRI and CT images for all performance metrics, the proposed approach demonstrated superior quantitative performance compared to traditional methods. This Quantitative evaluation helps confirm the effectiveness and generalizability of the methods or models across different methods.

Doi : https://doi.org/10.54216/JCIM.140205
Received: January 17, 2024 Revised: March 18, 2024 Accepted: July 02, 2024

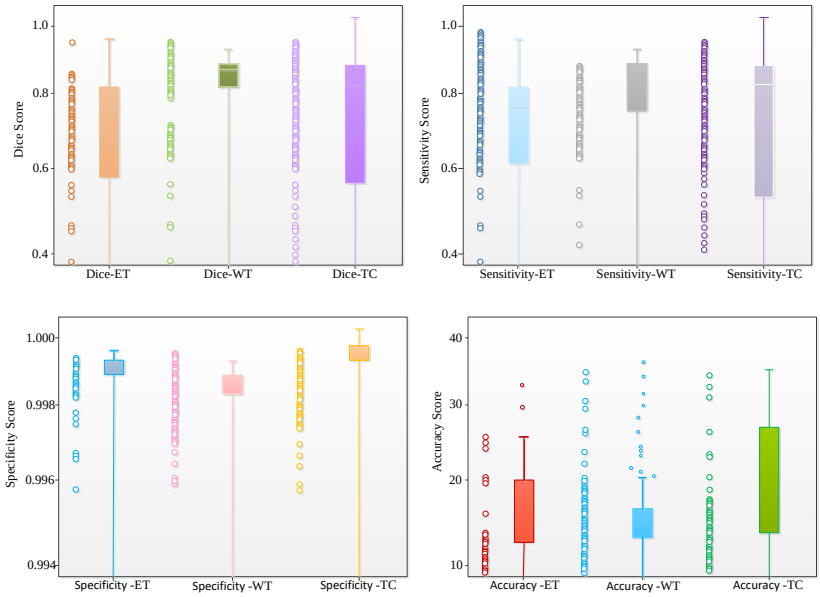

Figure 5: shows the ET, TC, and WT performance in DSC, Sensitivity, Specificity and Accuracy of our method

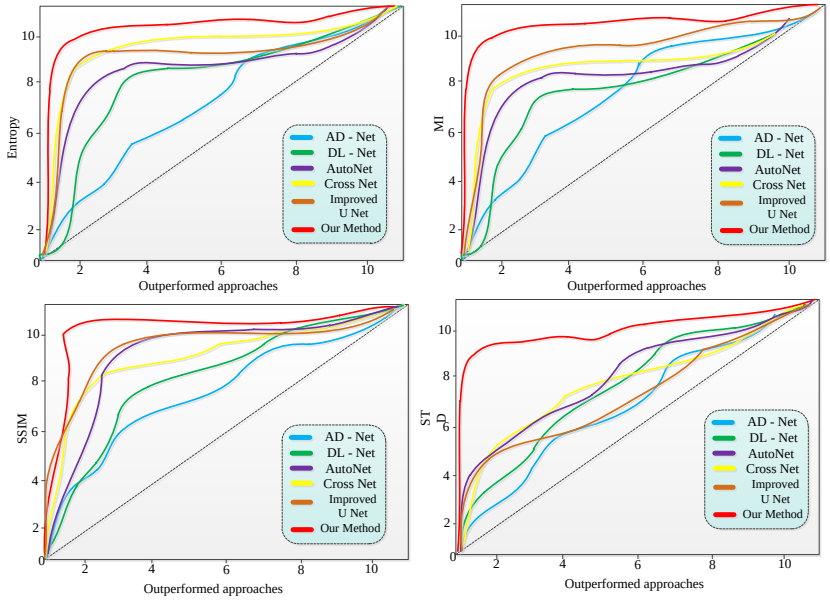

Figure 6: shows the outperformed conventional approaches in terms of quantitative performance

Table 3: shows the comparison of The MRI and CT image fusion is assessed with the existing methods

Methods	Accuracy	Specificity	Sensitivity	DSC
AD-Net	95.36	94.77	93.77	92.47
DL-Net	96.24	95.78	94.36	94.65
AutoNet	94.88	95.55	95.78	94.44

Doi : https://doi.org/10.54216/JCIM.140205
Received: January 17, 2024 Revised: March 18, 2024 Accepted: July 02, 2024

CrossNet	97.25	96.77	96.02	93.92
Improved-U-Net	97.68	97.15	95.65	91.32
Our method	98.65	97.68	96.25	95.36

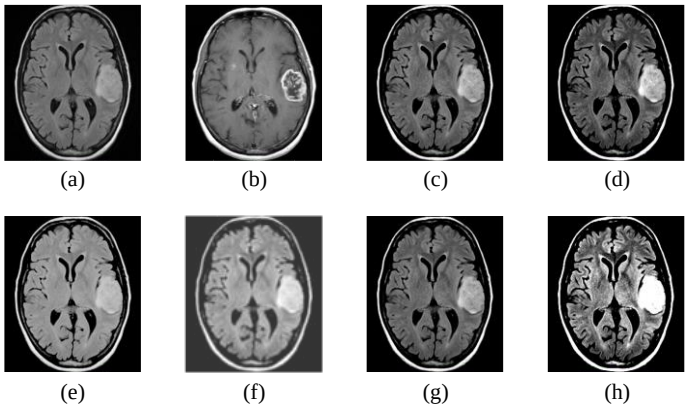

Figure 7: represents the MRI-CT fusion a) MRI image b) CT- image c) AD-Net d) DL-Net e) AutoNet f) CrossNet g) Improved-U-Net h) Our method.

Table 4 represents the comparison of objectives of the proposed framework with the state-of-the-art-methods and it is performed for analysing the effectiveness of the segmentation and considering the factors such as quality of image, content information, similarity in structures and consistency for segmenting result. Fig 8: comparison of the segmentation performance of CT, MRI and fused images. The objectives which we use for the comparison are ETP (Entropy), PSNR (Peak Signal-To-Noise Ratio), MI (Mutual Information), SSIM (Structural Similarity Index), STD (Standard Deviation).

Table 4: represents the comparison of objectives of the proposed framework with the state-of-the-art-methods

Metrices	AD-Net	DL-Net	AutoNet	CrossNet	Improved-U-Net	Our method
ETP	6.734	6.5588	6.324	7.598	8.369	10.997
PSN	26.	35.	41.	43.	48.	49.

Doi : https://doi.org/10.54216/JCIM.140205
Received: January 17, 2024 Revised: March 18, 2024 Accepted: July 02, 2024

R	3 5 8	6 9 8	2 5 9	6 5 8	3 7 8	5 7 8
MI	0 . 5 9 8 7	0 . 6 5 8 7	0 . 2 6 5	1 . 2 6 8	1 . 9 8 7	2 . 3 5 9
SSIM	0 . 2 5 7	0 . 8 9 7	0 . 3 5 7	0 . 4 8 7	0 . 6 8 9	0 . 9 8 7
STD	0 . 2 5 8	0 . 2 1 5 8	0 . 2 0 1 7	0 . 2 5 9 1	0 . 0 2 3 4	0 . 2 7 9 8

5. Conclusion

BT are unusual growths of brain cells which can be malignant or benign and it can be occurred from different types of brain cells. The process of locating and evaluating anomalies in the brain which can point to the condition of a tumor is known as brain tumor detection. Malignant tumors have a greater potential to spread, since benign tumors normally develop slowly and have identifiable borders. Tumor characteristics affect the symptoms that might mimic other disorders and demand a perfect medical evaluation for a relevant diagnosis. Critical information for diagnosis and therapy planning is provided by imaging methods such as PET and MRI. We used MRI and CT modalities to segment the BT using a novel framework LSTM-Auto encoder-based NAS which extracts relevant features from the input modalities. Ideal preprocessing methods like noise reduction, normalization, and bias correction are utilized has been performed for removing the artifacts which helps in accurately segmenting the BT. Spatial and temporal aspects of the tumor are occupied by the performed methods. Moreover, the SGR used in this approach promotes segmentation accuracy, while the CIM encourages multi-modal data integration. Dice coefficient, sensitivity, specificity, and accuracy are evaluated and our method obtained 98.65, 97.68, 96.25 and 95.36. while comparing with the several network contexts using the MRI and CT images. Additionally, by comparing the overall performance of our work with other existing work our work shows a better performance measure. Overall, our method promotes BT segmentation accuracy by utilizing neural network architectures and image processing techniques to promote treatment outcomes and patient management.

References

[1] Zheng, P., Zhu, X., & Guo, W. (2022). Brain tumour segmentation based on an improved U-Net. BMC Medical Imaging, 22(1), 199.

[2] Roy, S., Saha, R., Sarkar, S., Mehera, R., Pal, R. K., & Bandyopadhyay, S. K. (2023). Brain tumour segmentation using S-Net and SA-Net. IEEE Access, 11, 28658-28679.

[3] Ambeth Kumar, V.D. (2017). Automation of Image Categorization with Most Relevant Negatives. Pattern Recognition and Image Analysis, 27(3), 371–379.

[4] Kumar, I., Kumar, A., Kumar, V.D.A. et al. (2022) Dense Tissue Pattern Characterization Using Deep Neural Network. Cogn Comput 14, 1728–1751.

[5] Jiang, Y., Zhang, Y., Lin, X., Dong, J., Cheng, T., & Liang, J. (2022). SwinBTS: A method for 3D multimodal brain tumor segmentation using swin transformer. Brain sciences, 12(6), 797.

[6] Lin, J., Lin, J., Lu, C., Chen, H., Lin, H., Zhao, B., ... & Han, C. (2023). CKD-TransBTS: clinical knowledge-driven hybrid transformer with modality-correlated cross-attention for brain tumor segmentation. IEEE transactions on medical imaging.

Doi : https://doi.org/10.54216/JCIM.140205
Received: January 17, 2024 Revised: March 18, 2024 Accepted: July 02, 2024

[7] Zou, K., Yuan, X., Shen, X., Wang, M., & Fu, H. (2022, September). Tbrats: Trusted brain tumor segmentation. In International Conference on Medical Image Computing and Computer-Assisted Intervention (pp. 503-513). Cham: Springer Nature Switzerland.

[8] Ladkat, A. S., Bangare, S. L., Jagota, V., Sanober, S., Beram, S. M., Rane, K., & Singh, B. K. (2022). Deep neural network-based novel mathematical model for 3D brain tumor segmentation. Computational Intelligence and Neuroscience, 2022.

[9] Kumar, V.D.A., Sharmila, S., Kumar, A. et al. (2023). A novel solution for finding postpartum haemorrhage using fuzzy neural techniques. Neural Comput & Applic. 35(33), 23683–23696

[10] Yan, C., Ding, J., Zhang, H., Tong, K., Hua, B., & Shi, S. (2022). SEResU-Net for multimodal brain tumor segmentation. IEEE Access, 10, 117033-117044.

[11] Musallam, A. S., Sherif, A. S., & Hussein, M. K. (2022). A new convolutional neural network architecture for automatic detection of brain tumors in magnetic resonance imaging images. IEEE access, 10, 2775-2782.

[12] Sathya Preiya, V., and V. D. Ambeth Kumar. (2023). Deep Learning-Based Classification and Feature Extraction for Predicting Pathogenesis of Foot Ulcers in Patients with Diabetes. Diagnostics 13(12), 1983.

[13] Subramanian, S., Ghafouri, A., Scheufele, K. M., Himthani, N., Davatzikos, C., & Biros, G. (2022). Ensemble inversion for brain tumor growth models with mass effect. IEEE Transactions on Medical Imaging, 42(4), 982-995.

[14] Guan, X., Yang, G., Ye, J., Yang, W., Xu, X., Jiang, W., & Lai, X. (2022). 3D AGSE-VNet: an automatic brain tumor MRI data segmentation framework. BMC medical imaging, 22, 1-18.

[15] Thompson, B. H., Di Caterina, G., & Voisey, J. P. (2022, March). Pseudo-label refinement using superpixels for semi-supervised brain tumour segmentation. In 2022 IEEE 19th International Symposium on Biomedical Imaging (ISBI) (pp. 1-5). IEEE.

[16] Khairandish, M. O., Sharma, M., Jain, V., Chatterjee, J. M., & Jhanjhi, N. Z. (2022). A hybrid CNN-SVM threshold segmentation approach for tumor detection and classification of MRI brain images. Irbm, 43(4), 290-299.

[17] Balakrishnan, Chitra, and V. D. Ambeth Kumar. (2023). IoT-Enabled Classification of Echocardiogram Images for Cardiovascular Disease Risk Prediction with Pre-Trained Recurrent Convolutional Neural Networks. Diagnostics 13(4), 775

[18] Rajaragavi, R., & Rajan, S. P. (2022). Optimized U-Net Segmentation and Hybrid Res-Net for Brain Tumor MRI Images Classification. Intelligent automation & soft computing, 32(1).

[19] Hemamalini, Selvamani, and Visvam Devadoss Ambeth Kumar. (2022). Outlier Based Skimpy Regularization Fuzzy Clustering Algorithm for Diabetic Retinopathy Image Segmentation. Symmetry, 14(12), 2512

[20] Ejaz, K., Suaib, N. B. M., Kamal, M. S., Rahim, M. S. M., & Rana, N. (2023). Segmentation Method of Deterministic Feature Clustering for identification of brain tumor using MRI. IEEE Access.

[21] Sheela, C. J. J., & Suganthi, G. (2022). Automatic brain tumor segmentation from MRI using greedy snake model and fuzzy C-means optimization. Journal of King Saud University-Computer and Information Sciences, 34(3), 557-566.

[22] Ferdous, G. J., Sathi, K. A., Hossain, M. A., Hoque, M. M., & Dewan, M. A. A. (2023). LCDEiT: A linear complexity data-efficient image transformer for MRI brain tumor classification. IEEE Access, 11, 20337-20350.

[23] Ambeth Kumar, V.D. Ramakrishnan,M. (2013). Temple and Maternity Ward Security using FPRS. Journal of Electrical Engineering & Technology, 8(3), 633-637.

[24] Asif, S., Yi, W., Ain, Q. U., Hou, J., Yi, T., & Si, J. (2022). Improving effectiveness of different deep transfer learning-based models for detecting brain tumors from MR images. IEEE Access, 10, 34716-34730.

[25] Zhu, Z., He, X., Qi, G., Li, Y., Cong, B., & Liu, Y. (2023). Brain tumor segmentation based on the fusion of deep semantics and edge information in multimodal MRI. Information Fusion, 91, 376-387.

[26] Sherubha, "Graph Based Event Measurement for Analyzing Distributed Anomalies in Sensor Networks", Sådhanå(Springer), 45:212, https://doi.org/10.1007/s12046-020-01451-w

Doi : https://doi.org/10.54216/JCIM.140205
Received: January 17, 2024 Revised: March 18, 2024 Accepted: July 02, 2024

[27] Piyush K. Pareek, Pixel Level Image Fusion in Moving objection Detection and Tracking with Machine Learning ",Fusion: Practice and Applications, Volume 2 , Issue 1 , PP: 42-60, 2020

[28] Shivam Grover, Kshitij Sidana, Vanita Jain, "Egocentric Performance Capture: A Review", Fusion: Practice and Applications, Volume 2, Issue 2 , PP: 64-73, 2020.

[29] Abdel Nasser H. Zaied, Mahmoud Ismail and Salwa El- Sayed, A Survey on Meta-heuristic Algorithms for Global Optimization Problems, Journal of Intelligent Systems and Internet of Things,Volume 1 , Issue 1 , PP: 48-60, 2020

[30] Mahmoud H.Alnamoly, Ahmed M. Alzohairy, Ibrahim M. El-Henawy, "A survey on gel images analysis software tools, Journal of Intelligent Systems and Internet of Things,Volume 1 , Issue 1 , PP: 40-47, 2021.

Doi : https://doi.org/10.54216/JCIM.140205
Received: January 17, 2024 Revised: March 18, 2024 Accepted: July 02, 2024